ELSEVIER

A highly active and stable single-atom catalyst for oxygen reduction with axial Fe-O coordination prepared through a fast medium-temperature pyrolysis process

Qingqing Wang [a,b,1], Guifa Long [c,1], Xiaohong Gao [a], Jieli Chen [a], Chenghang You [a,*], Xinlong Tian [a,*], Xianghui Wang [b], Dulin Kong [d], Wenjun Fan [e,*]

[a] State Key Laboratory of Marine Resource Utilization in South China Sea, Hainan Provincial Key Lab of Fine Chemistry, School of Chemical Engineering and Technology, Hainan University, Haikou 570228, China
[b] Key Laboratory of Water Pollution Treatment and Resource Reuse of Hainan Province, School of Chemistry and Chemical Engineering, Hainan Normal University, Haikou 571158, China
[c] Guangxi Key Laboratory of Chemistry and Engineering of Forest Products, School of Chemistry and Chemical Engineering, Guangxi Minzu University, Nanning 530008, China
[d] Key Laboratory of Tropical Translational Medicine of Ministry of Education, Hainan Provincial Key Laboratory for Research and Development of Tropical Herbs, Haikou Key Laboratory of Li Nationality Medicine, School of Pharmacy , Hainan Medical University, 571199 Haikou, Hainan, China
[e] Dalian National Laboratory for Clean Energy, State Key Laboratory of Catalysis, iChEM, Dalian Institute of Chemical Physics, Chinese Academy of Sciences, Dalian 116023, China

ARTICLE INFO

ABSTRACT

In this study, we developed a highly active and stable Fe single atomic catalyst with axial Fe–O coordination through a fast medium-temperature pyrolysis process. The catalyst exhibited a high ORR performance, with a high half-wave potential of 0.93 V (vs. RHE), as well as excellent stability. When incorporated in a zinc–air battery's air electrode, a high power density of 214.5 mW cm^{-2} was obtained. After 333 h cyclic charging-discharging test, no obvious performance decay was observed. Density functional theory calculations revealed that the axial Fe–O coordination optimized the interactions between Fe and intermediates, inhibited the demetallization of Fe single atomic active sites and eventually enhanced the performance and stability of the obtained catalyst. We believe that the present strategy is easily translatable to the rational design of highly active and stable ORR catalysts for eco-friendly and future-oriented energy applications.

1. Introduction

The oxygen reduction reaction (ORR) plays a key role in several advanced renewable energy conversion technologies, such as proton exchange membrane fuel cells (PEMFCs), direct methanol fuel cells (DMFCs), and metal–air batteries [1–12]. Highly active catalysts are required to overcome the sluggish kinetics of ORR. To date, Pt-based catalysts are the state-of-the-art ORR catalysts. However, their scarcity, high cost, and inferior stability have hampered their large-scale application. Therefore, the development of highly active, stable, and low-cost ORR catalysts is crucial for further progress in the scale-up of advanced energy technologies.

Carbon-based single atomic catalysts with Fe-N4 active sites (Fe-

SAC) have attracted significant attention owing to their high ORR performance, unique quantum size effect, and nearly 100% atomic utilization [13–16]. However, the reported Fe-SACs still fail to meet practical demands. On the one hand, the adsorption of the intermediates formed during the ORR procedure at Fe sites is too strong, making the intermediates hard to desorb and blocking the refreshments of the active sites. On the other hand, the FeN4 structures are prone to demetallization during the ORR procedures, resulting in reduced catalytic performance and even deactivation[17,18]. To further enhance the performance of Fe-SAC, the electronic structure of the Fe centers, needs to be modified to inhibit those unfavorable interactions with the intermediates during the ORR [19–24]. Introducing extra axial O coordination is recently discovered to be a direct and effective way to reduce

---

the electron density of Fe single atoms, favor the desorption of intermediates during the ORR process, and eventually enhance the performance of Fe-SAC [25,26].

Generally, high-temperature pyrolysis (>500 °C) is required to improve the stability of carbon-based catalysts[27–29]. However, during the pyrolysis procedures at such high temperatures, the doped O atoms will be removed with the nearby C atoms, rendering the precise control of the content and types of O atoms unachievable and eventually hindering the successful coordination between O and Fe sites [30,31]. Additionally, because controlling the pyrolysis process at high temperatures is challenging, the compositions and structures of the final catalysts are random and complex. Specially, the high temperature intensify the metal aggregation, leading to the formation of undesirable metal nanoparticles, which also hampers the formation of single atom sites and make it difficult to study the structure-performance relationships of the catalysts obtained[23]. Therefore, achieving stable coordination between O atoms and Fe sites at lower temperatures is an attractive yet challenging mission.

In this study, we developed an effective strategy for the preparation of a highly active and stable Fe-SAC with an axial Fe–O coordination through a fast medium-temperature pyrolysis process. The obtained axially coordinated Fe-SAC exhibited a high ORR performance, with a half-wave potential as high as 0.93 V (vs. RHE), which is among the highest values reported to date. In addition, the catalyst exhibited outstanding stability. After 50000 s of continuous operation at 0.62 V (vs. RHE), no obvious performance decay was observed. When used as the air electrode catalyst in a zinc–air battery (ZAB), the ZAB achieved a high power density of 214.5 mW cm^{-2}. Density functional theory (DFT) calculations reveal that the introduced axial Fe–O coordination not only modified the electron structures of Fe single atoms and facilitated ORR but also inhibited the demetallization of Fe single atomic active sites and eventually enhanced the stability of Fe-SAC. The high performance and stability of this catalyst make it suitable for practical and commercial applications. Also, we believe that the present strategy can be easily translated into the rational design and fabrication of ORR catalysts with both high activity and stability for eco-friendly and future-oriented energy techniques.

2. Experimental

2.1. Preparation of precursors

1.00 g of carbon black (C, Vulcan XC-72R) and specific amounts of iron phthalocyanine (FePc, Sigma-Aldrich) were placed in an agate mortar. After thorough grinding and mixing, the precursors were obtained and labeled as "C/mFePc," where the number "m" represents the weight percent of FePc (m =5, 10, 20). Since the surface of the commercial carbon black itself has plenty of oxygen-containing groups, perhaps due to the prolonged exposure to air, no additional oxygen was introduced during the preparation of the catalyst.

2.2. Preparation of catalysts

The obtained precursor was placed in a tube furnace and heated at 350 °C for 30 min under an N$_2$ atmosphere (Fig. 1). After cooling naturally to room temperature, the final catalysts were obtained and labeled C/mFePc-350, where "350" refers to the applied temperature.

3. Results and discussions

3.1. Structural characterization of catalysts

To analyze the porous structures of the obtained catalysts, the N$_2$ adsorption-desorption isotherms were recorded (Fig. 2a) and the corresponding BET surface areas were calculated (Fig. 2b). C and C-350 had similar BET surface areas, as well as similar external surface and micropore areas, suggesting that the medium temperature pyrolysis applied can hardly affect the porous structures of the carbon matrix. When FePc was added, the surface area decrease to 201 m^2 g^{-1}. The decreased external surface area and similar micropore area to C suggest that the FePc addition mainly affect the external surface area, for which the coverage of FePc on the surface of C should be properly responsible. When C/10FePc was heated, it was interesting to find that the micropore area decreased sharply to 19 m^2 g^{-1}, while no obvious changes in the external surface area was observed. As a result, C/10FePc-350 has a BET surface area of only 121 m^2 g^{-1}.

To identify the structural features at the atomic level, aberration-corrected high-angle annular dark-field scanning transmission electron microscopy (AC-HAADF-STEM) was used (Fig. 3b). As illustrated in Fig. 3a, numerous isolated bright dots can be seen in C/10FePc-350, which are corresponding to the atomically and homogeneously dispersed Fe single atoms. The energy dispersive X-ray spectroscopy (EDX) mapping results revealed that the C, N, O, and Fe atoms were homogeneously distributed in C/10FePc-350 (Fig. 3b to f).

To explore the surface compositions and chemical states of the elements in the catalysts, we conducted X-ray photoelectron spectroscopy (XPS) (Fig. S1 and Table S1). To further study the exact atomic composition of O and Fe, high-resolution O1s and Fe2p spectra were recorded and deconvoluted. Fig. 4a, b, and Table S2 show the high-resolution O1s spectra and atomic compositions of different O species in the various catalysts. C–O accounts for 76.1 and 86.4 at% in C and C/10FePc, respectively, suggesting that the main O species in C and C/10FePc is C–O. After heat treatment, the C–O content in the two catalysts decreased drastically to 32.6 and 24.9 at%, respectively, while the C=O content increased from 23.9 and 13.6–67.4% and 68.2%, respectively (Table S2). These changes in the atomic contents of the O species suggest that the C–O structures in C and C/10FePc were partially decomposed or transformed into C=O during the heat-treatment. Particularly, in the O1s spectrum of C/10FePc-350, a Fe–O peak was seen around 530.5 eV in addition to C–O and C=O peaks, suggesting the existence of the coordination between O and Fe[32]. Considering the disappearance of the Fe–O peak in C/10FePc, the formation of Fe–O bonds could be only
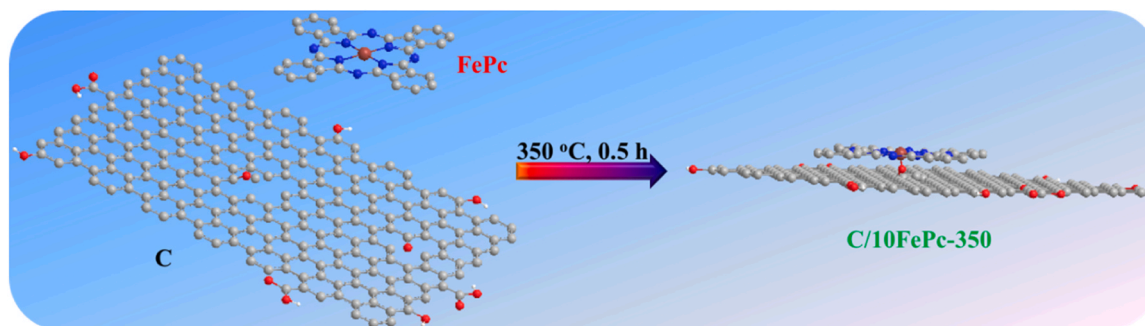

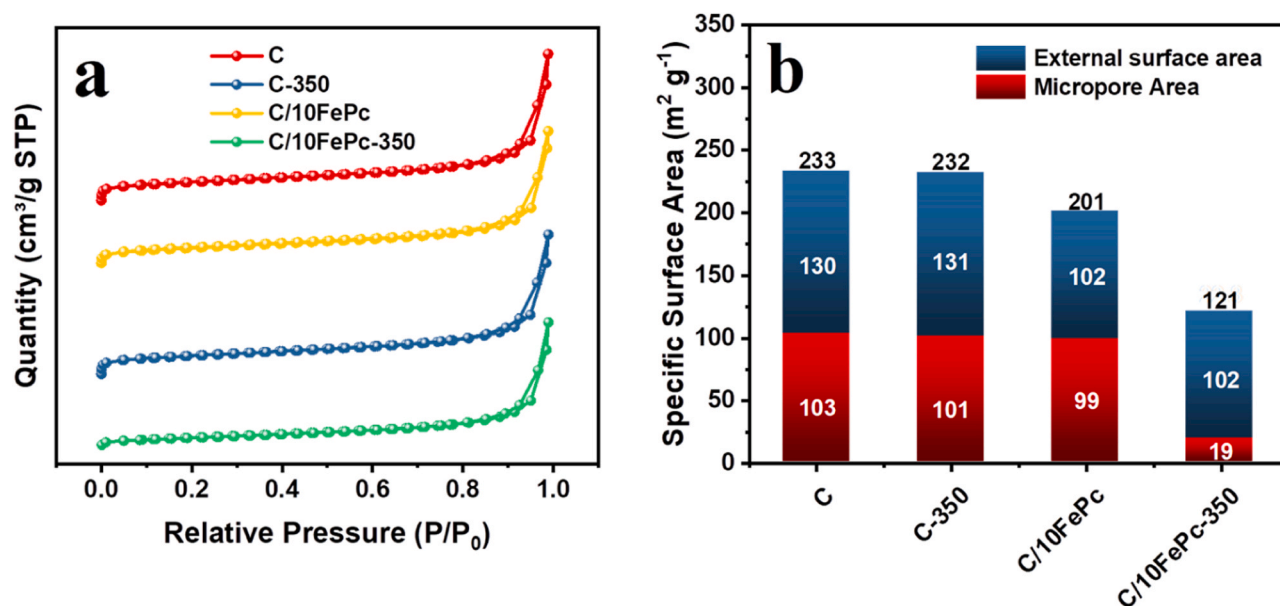**Fig. 1.** Schematic diagram of the synthesis for C/10FePc-350.

Fig. 2. N_2 adsorption-desorption isotherms for various catalyst; (b) BET surface areas and corresponding external surface and micropore area (derive from the t-plot results) of the obtained catalysts.
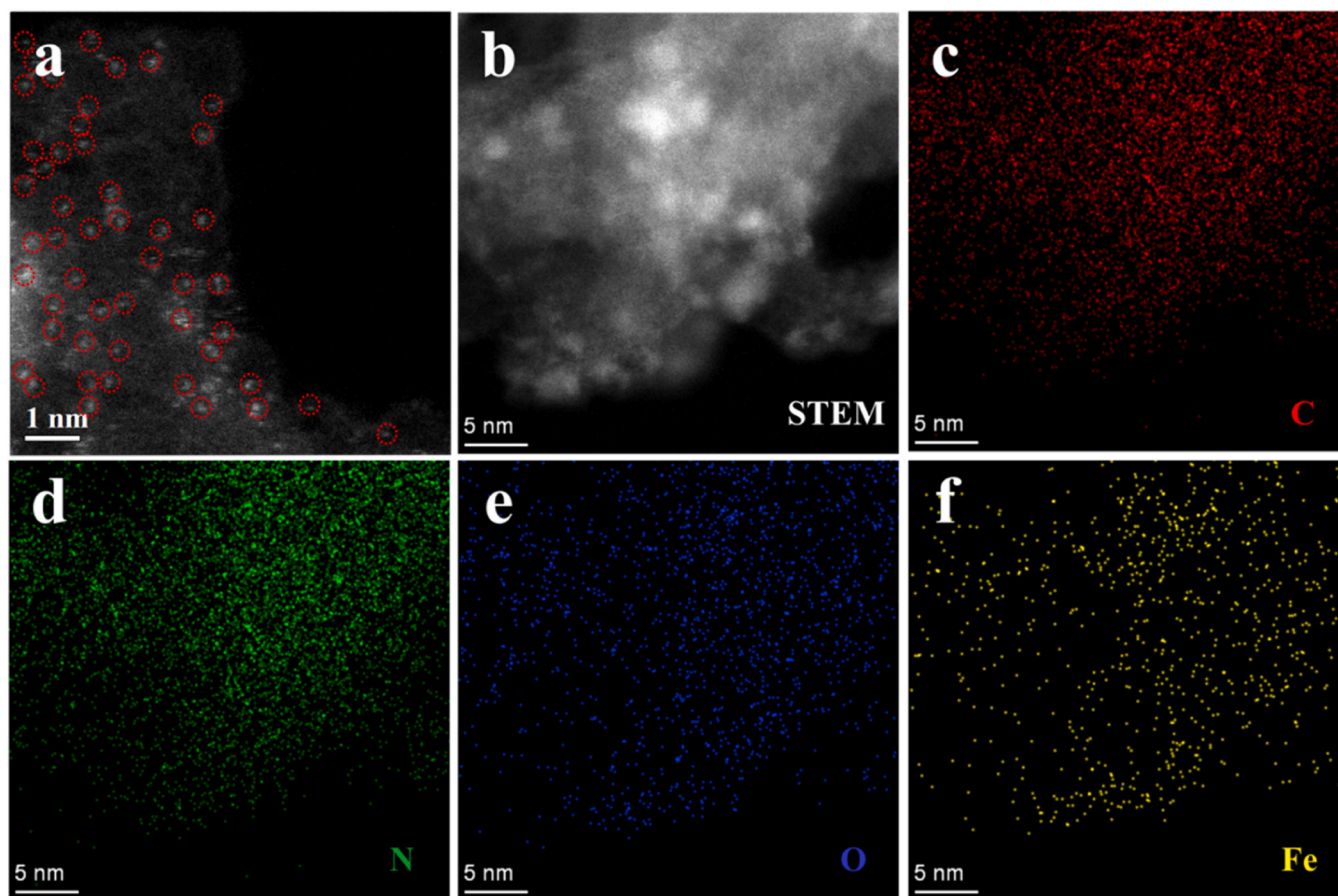

Fig. 3. (a) AC HAADF-STEM images of C/10FePc-350, with the Fe atoms marked by red circles; (b) STEM image; (f) EDX mapping of C, N, O, and Fe in C/10FePc-350.

triggered by the assistance of medium-temperature pyrolysis. Fig. 4c shows the Fe2p spectrum and relative deconvolution results of C/10FePc and C/10FePc-350. In the C/10FePc spectrum, the four peaks

at 728.5, 723.7, 715.2, and 710.1 eV were assigned to the satellite (Sat.) (2p1/2), Fe^{2+} (2p1/2), Sat. (2p3/2), and Fe^{2+} (2p3/2) peaks, respectively. Similarly, four peaks were observed in the Fe2p spectrum of
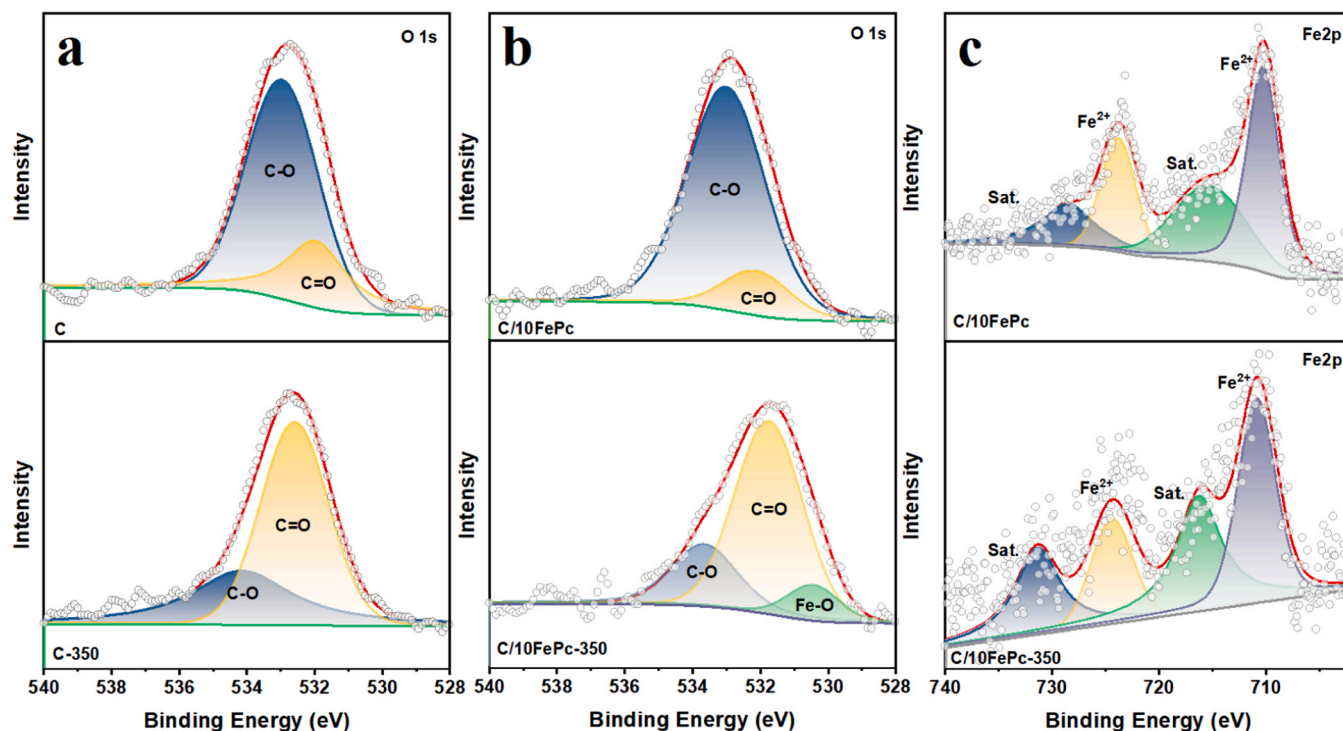
Fig. 4. High-resolution XPS spectra: (a) O1s spectra of C (top) and C-350 (bottom); (b) O1s spectra of C/10FePc (top) and C/10FePc-350 (bottom); (c) Fe2p spectra of C/10FePc (top) and C/10FePc-350 (bottom).

C/10FePc-350. After pyrolysis, the binding energies of Fe^{2+} (2p1/2) and Fe^{2+} (2p3/2) shifted positively to 724.3 and 710.8 eV, respectively, suggesting a sparser electron density around Fe^{2+} in C/10FePc-350, which can be also attributed to the additional coordination of Fe and O.

To obtain further information on the coordination state of Fe in C/10FePc-350, X-ray absorption near-edge structure (XANES) and extended X-ray absorption fine structure (EXAFS) analyses were performed. Fig. 5a shows the XANES spectra of Fe in the various materials. The Fe absorption value in C/10FePc-350 is between those of FePc and Fe_2O_3 (the magnified figure inserted in Fig. 5a), suggesting that the valence state of Fe in C/10FePc-350 is between + 2 and + 3, which can be also confirmed by the white line peak intensity between FePc and Fe_2O_3. The absence of a Fe–Fe peak near 2.16 Å in the Fourier-transform EXAFS (FT-EXAFS) spectra (Fig. 5b) of C/10FePc-350 indicates that there is no Fe–Fe bonds in C/10FePc-350, confirming that Fe in C/10FePc-350 exists as single atoms. Moreover, the FT-EXAFS results of FePc and C/10FePc-350 show that the Fe peak in C/10FePc-350 shifts negatively from 1.59 Å (FePc) to 1.45 Å (C/10FePc-350), indicating that the average bond length between Fe and surrounding atoms in C/10FePc-350 is shorter than that of FePc, which can be also verified by the wavelet-transform EXAFS (WT-EXAFS) results (Fig. 5c, d), with the signal center of Fe shifting positively from 4.27 (FePc) to 4.46 (C/10FePc-350).

The fitting parameters of Fe K-edge EXAFS (Table S3) revealed that the coordination number of Fe in C/10FePC-350 was close to 5 (4.9), implying that there are five ligands around Fe. Combining with the XPS results, a Fe-O bond in the axial direction of the FeN4 plane can be verified. That is, FePc in C/10FePc-350 is bonded to the carbon matrix through a Fe-O bond.

3.2. Electrocatalytic ORR performance of catalysts

To evaluate the ORR performance of the catalysts, cyclic voltammetry (CV) and linear sweep voltammetry (LSV) curves were recorded in O_2-saturated 0.1 M KOH solution. It can be seen that the pure C or FePc exhibited poor ORR catalytic performance, with peak potentials of 0.75

and 0.81 V (vs. RHE), respectively (Fig. 6a). Compared with FePc or C, C/10FePc exhibited a much higher ORR performance (Fig. 6a), with the peak potential shifting positively by 110 mV compared with pure FePc (Fig. 6a), which can be attributed to the improved conductivity induced by the incorporation of C. Among the obtained catalysts, C/10FePc-350 exhibited the highest peak potential of 0.94 V (vs. RHE), indicating its highest performance among the four catalysts. Similarly, C/10FePc-350 exhibited the highest ORR performance in the LSV experiments, with the highest half-wave potential of 0.93 V (vs. RHE) among the four catalysts (Fig. 6b and c), 50 mV more positive than that of Pt/C. To the best of our knowledge, it also ranks among the highest values of recently reported ORR catalysts (Table S4).

Tafel slope analyses were performed to investigate the ORR kinetics. As illustrated in Fig. 6d, C/10FePc-350 exhibited the lowest Tafel slope (11.1 mV dec^{-1}) among the synthesized catalysts, indicating that its ORR kinetics is the fastest compared to C/10FePc and FePc. To further investigate the ORR electron transfer pathways in the synthesized catalysts, we recorded the LSV curves under different rotation rates and calculated the electron transfer numbers of the various catalysts from the Koutecky–Levich (K-L) plots (Fig. 6e) derived from the LSV curves under different rotating rates (Fig. S2). Among the obtained catalysts, C/10FePc-350 had the highest electron transfer number of 4.05 (Fig. 6f), followed by 3.74. 3.43 and 2.91 for C/10FePc, FePC, and C, respectively, indicating that C/10FePc-350 has an ORR pathway close to the ideal four-electron pathway, which suggests that C/10FePc-350 has a superior ORR catalytic efficiency.

As the electrochemically active specific surface area (ECSA) is usually considered important for ORR catalysts, the ECSAs of various catalysts were evaluated based on the double-layer capacitor (C_{dl}) calculated from the CV curves under different scanning rates (Fig. S3). Among the obtained four catalysts, C/10FePc-350 had the lowest C_{dl} and ECSA of 1.7 mF cm^{-2} and 42.5, respectively, which should be attributed to its lowest BET surface area among the four catalysts.

To evaluate the intrinsic activity of the active sites in C/10FePc and C/10FePc-350, their current densities were normalized by their specific BET surface areas or ECSAs. As illustrated in Fig. S4, the normalized
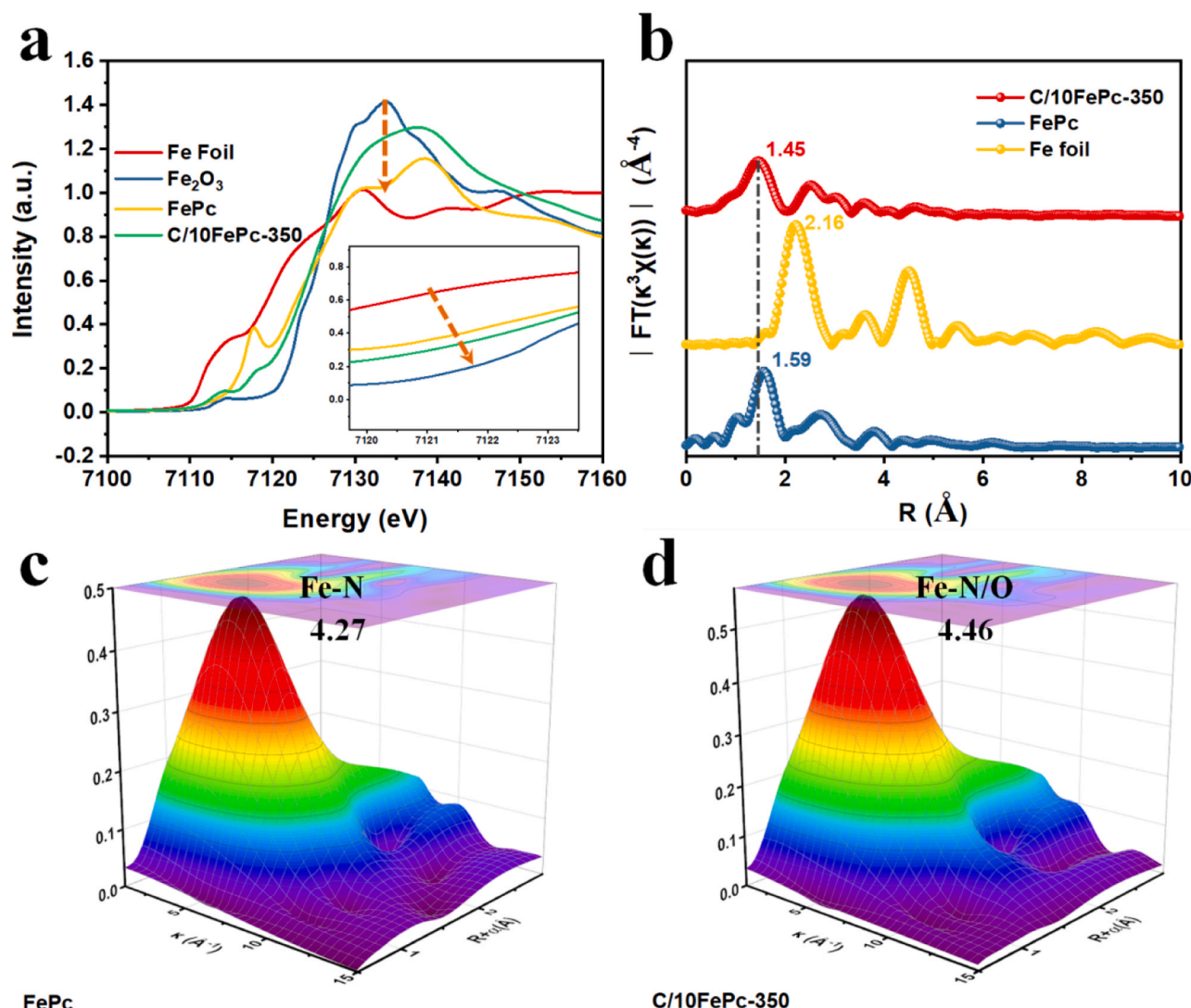
Fig. 5. (a) Fe K-edge XANES spectra; (b) FT-EXAFS spectra; WT-EXAFS: (c) FePc; (d) C/10FePc-350.

current densities of C/10FePc-350 were much higher than those of C/10FePc, suggesting that the intrinsic activity of the active sites in C/10FePc-350 was much higher than that in C/10FePc.

From the thermogravimetric (TG) curve (Fig. S5), it can be seen that FePc remained stable at 350 °C, with only slight loss of FePc upon the heat treatment. Hence, the FePc contents in C/10FePc and C/10FePc-350 were expected to be nearly the same. Thus, the significantly higher ORR performance of C/10FePc-350 is expected to be attributed to the FeN4O1 structures formed during the pyrolysis. In other words, the intrinsic catalytic performance of axially coordinated FePc, containing FeN4O1 structures, is much higher than that of FePc with only FeN4 structures.

To further confirm the high activity of the FeN4O1 structures, catalysts were prepared from precursors with different FePc contents. As the FePc content increased from 5 wt% to 10 wt%, the ORR performance of the catalyst was drastically enhanced (Fig. 6g and h), suggesting that the ORR enhancement of C/10FePc-350 stems from the increased FePc content. Interestingly, when the FePc content in the precursor was 20 wt %, the obtained catalyst's performance degraded, with half-wave potential shifting negatively to 0.90 V (Fig. 6g and h). We suggest the overlapping of FeN4O1 structures by excess FePc, which makes the as-formed FeN4O1 inaccessible and unable to catalyze the ORR, as the reason for this performance degradation of C/20FePc-350 (Fig. 7).

In addition to its high ORR performance, C/10FePc-350 also

exhibited excellent stability. After 50000 s continuous operation at 0.62 V (vs. RHE), C/10FePc-350 maintained 97.1% of its initial performance. C/10FePc, without axial Fe–O coordination, lost nearly 80% of its performance under the same test conditions (Fig. 6i), suggesting that axial Fe–O coordination can drastically enhance the stability of Fe-SAC.

3.3. Theoretical simulation of catalysts

To further investigate the mechanism of ORR and how the axial Fe–O coordination influences the reaction kinetics, the structure, and Gibbs free energy profiles for ORR over FeN4 and FeN4O1 were studied (Fig. 8, S6, and S7). Although the axial O coordination weakened the Fe–N bond by slightly decreasing its bond energy by 8.64 KJ mol^{-1} (from 245.76 to 237.12 KJ mol^{-1}), the total coordination bond energy (including four Fe–N bonds and one Fe–O bond) increased from 983.04 (FeN4) to 1052.16 KJ mol^{-1} (FeN4O1) due to the newly formed axial Fe–O coordination (Table S5). This higher total bond energy is believed to inhibit the demetallization process and enhance the stability of C/10FePc-350 (Fig. 6i).

Fig. 8a displays the mechanism of ORR, which involves five steps: 1) the adsorption of O_2 to the surface ($O_2 + * \rightarrow *O_2$); 2) the activation and protonation of adsorbed O_2 to form *OOH ($*O_2 + H_2O + e^- \rightarrow *OOH + OH^-$); 3) the formation of *O from *OOH ($*OOH + e^- \rightarrow *O + OH^-$); 4) the
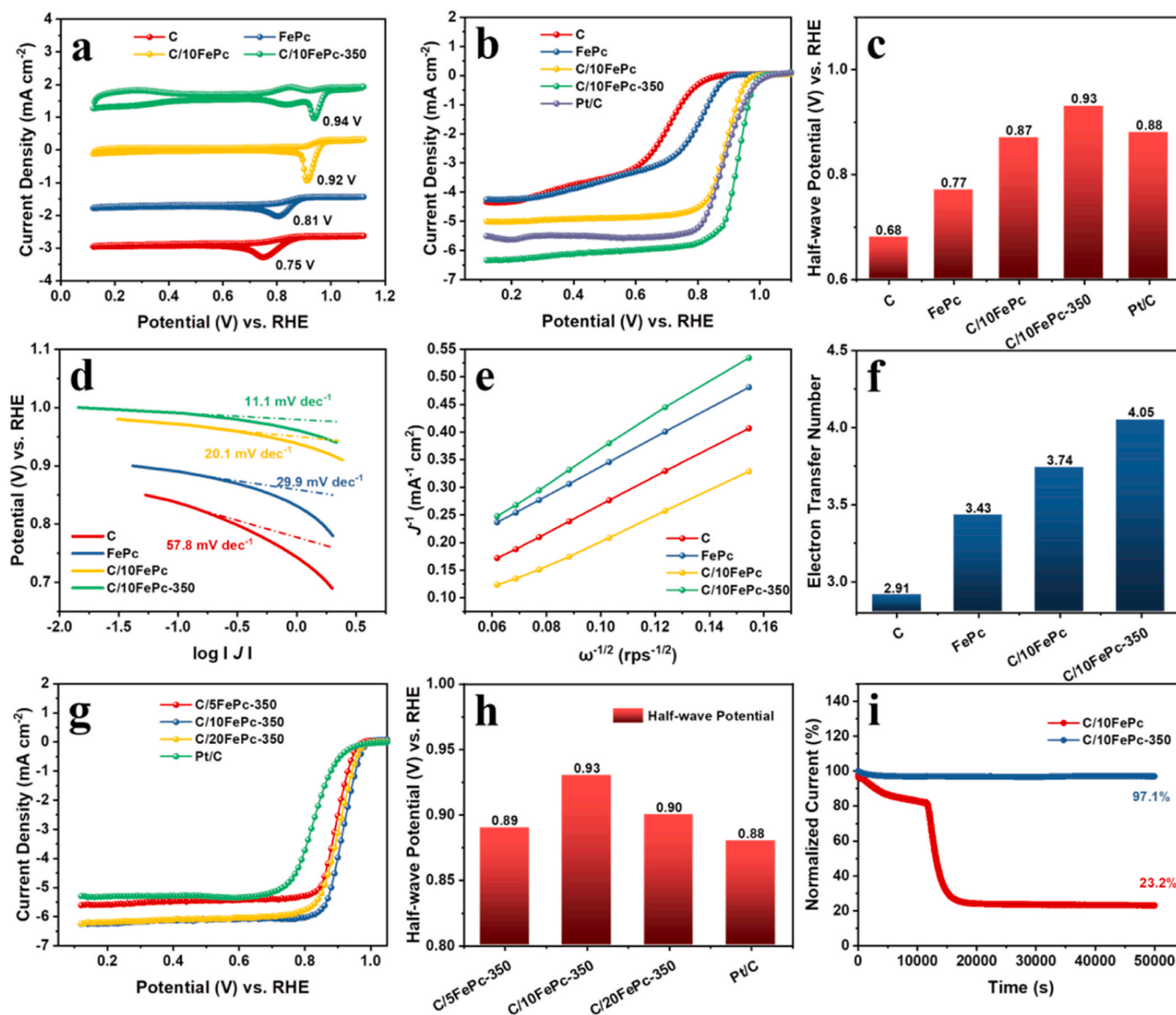
Fig. 6. (a) CV curves for various catalysts in O_2-saturated 0.1 M KOH solution at a scan rate of 5 mV s^{-1}; (b) LSV curves; (c) half-wave potentials derived from the LSV curves; (d) Tafel curves derived from the LSV curves; (e) K-L plots; (f) electron transfer number calculated from the K-L slopes; (g) LSV curves of catalysts prepared from precursors with different FePc contents; (h) half-wave potentials of C/5FePc-350, C/10FePc-350, and C/20FePc-350; (i) i-t curves for C/10FePc and C/10FePc-350.
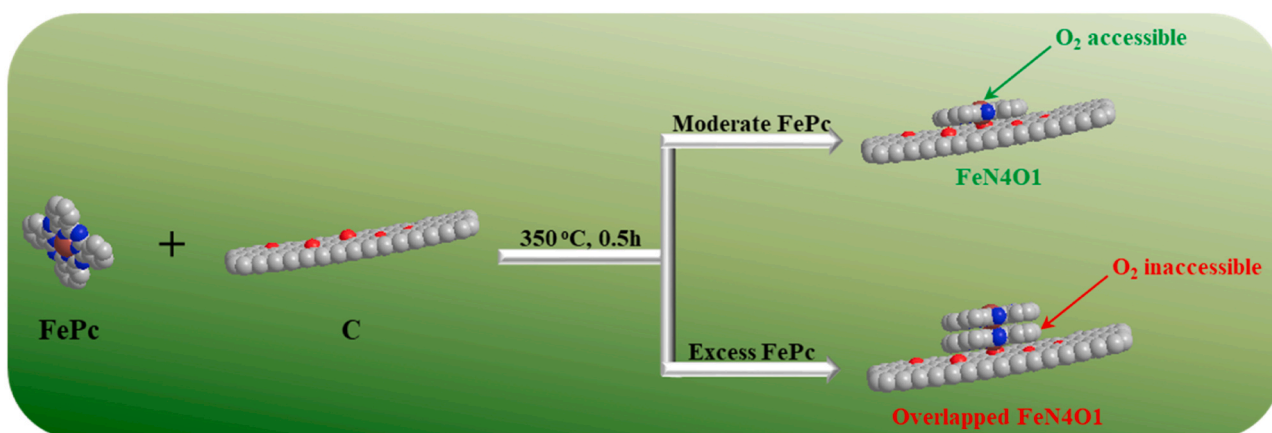

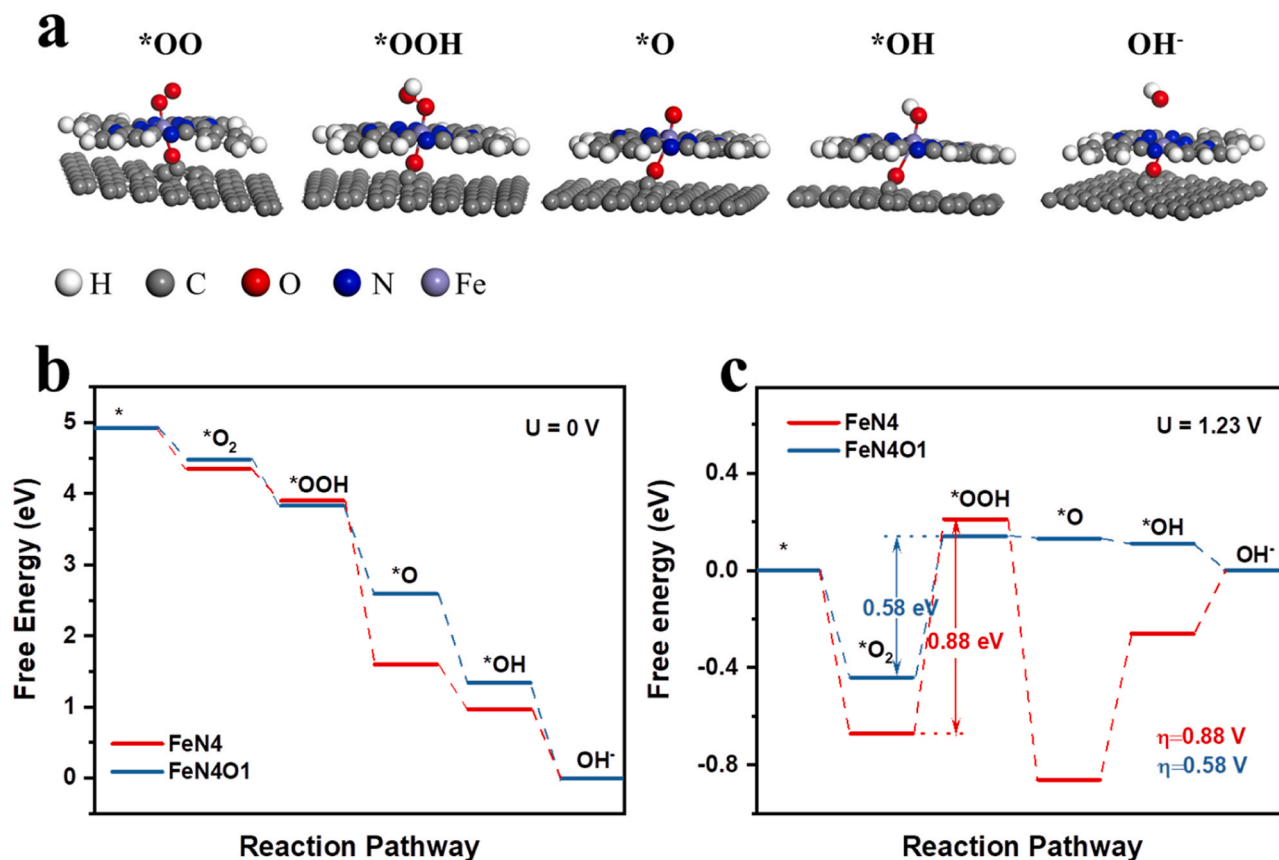**Fig. 7.** Schematic diagram of catalysts derived from precursors with different FePc contents.

Fig. 8. DFT results of the ORR activities of FeN4 and FeN4O1 sites: (a) Optimized structures of the intermediate species adsorbed on the FeN4O1 site in C/10FePc-350. The white, gray, red, blue, and grayish purple balls refer to hydrogen, carbon, oxygen, nitrogen, and iron atoms, respectively. (b) Free energy diagrams of the ORR pathways on FeN4 and FeN4O1 sites at U = 0 V. (c) Free energy diagrams of the ORR pathways on FeN4 and FeN4O1 sites at U = 1.23 V.

protonation of *O to form *OH (*O + H_2O + e^- → *OH + OH^-); and 5) the formation and desorption of OH^- from *OH (*OH + e^- → * + OH^-), which refreshes the active sites. Figs. 7b and 7c show the free energies of the

ORR pathways on FeN4 and FeN4O1 at U = 0 V and U = 1.23 V (Fig. 8b and c). The adsorption of OOH on FeN4O1 is easier and more stable than on FeN4, while the adsorption of *OH on FeN4O1 is weaker than on
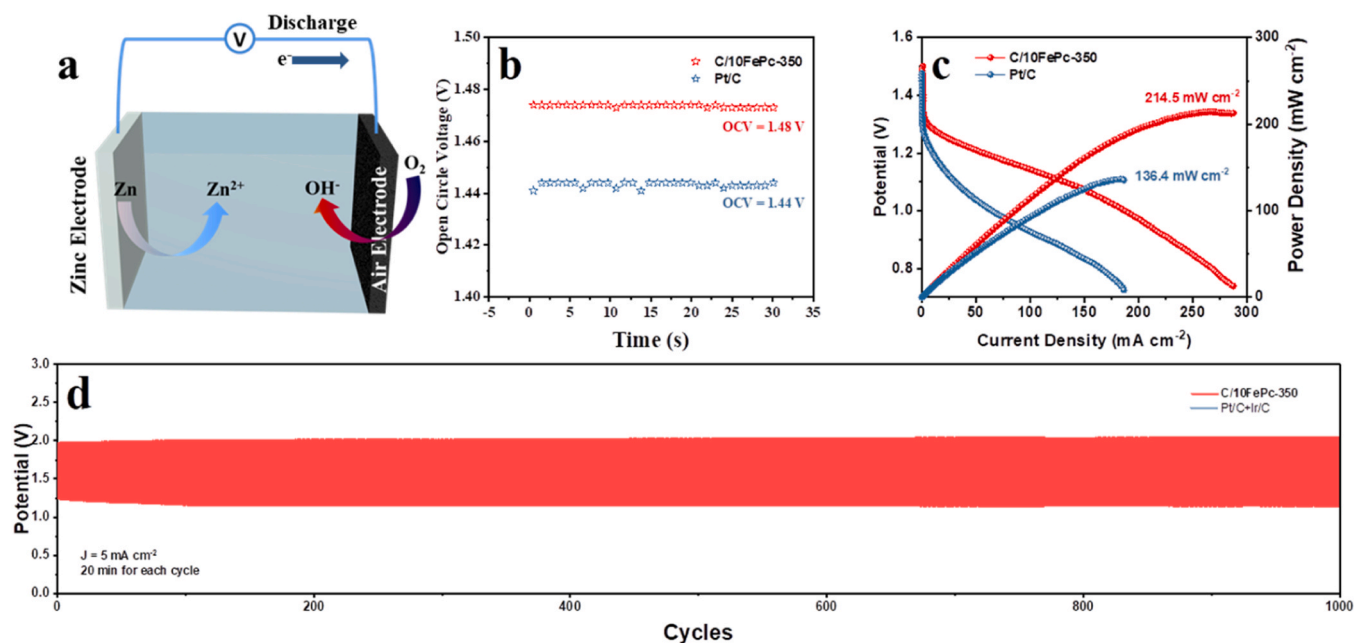

Fig. 9. (a) Schematic illustration of a primary aqueous ZAB during discharge; (b) Open circle potentials of ZABs using C/10FePc-350 and Pt/C as electrode catalysts; (c) discharge curves and the related power density plots; (d) cycling performance of the ZAB using C/10FePc-350.

FeN4. Hence, the formed OH can easily desorb from the active sites, leading to the easier renewal of active sites and facilitating the ORR process. The rate-determining steps of both FeN4O1 and FeN4 are the protonation of the adsorbed O_2 to form *OOH (*O_2 + H_2O + e^- → *OOH + OH^-). The corresponding overpotentials of ORR (η) on FeN4O1 and FeN4 are 0.58 and 0.88 V, respectively, which is in agreement with the superior ORR performance of FeN4O1 compared with FeN4. Based on these results, we attribute the modified electron structures induced by the axial Fe–O coordination to the ORR performance enhancement seen with C/10FePc-350.

3.4. Zn-air battery (ZAB) test

To further evaluate the potential of the catalyst for practical applications, a ZAB was fabricated using C/10FePc-350 as the air electrode catalyst (Fig. 9a). Fig. 9b and c show the open circle voltages (OCV), discharging curves, and corresponding power density curves of the ZABs with different catalysts. Compared with the baseline Pt/C catalyst, the ZAB with C/10FePc-350 delivered a higher performance reflected in its higher OCV, discharge current density, and power density (214.5 mW cm^{-2} at 250 mA cm^{-2}), which further confirms its excellent catalytic activity towards ORR. In addition to its high activity, C/10FePc-350 demonstrated excellent stability when used in ZAB. After 1000 cycles (corresponding to 333 h), only a slight decay in the discharge voltage was observed (Fig. 9d). We believe that this high ORR performance and excellent stability make C/10FePc-350 a potential candidate for practical applications.

4. Conclusions

In summary, we developed an effective strategy for the preparation of a highly active and stable Fe single atomic catalyst (Fe-SAC) with axial Fe-O coordination through a fast medium-temperature pyrolysis process. The obtained axially coordinated Fe-SAC exhibited a high ORR performance, with a half-wave potential as high as 0.93 V (vs. RHE), which is among the highest values recently reported. In addition, the catalyst exhibited outstanding stability. After 50,000 s of continuous operation, no obvious performance decay was observed. When used as an air electrode catalyst in a ZAB, it can give the ZAB a high power density of 214.5 mW cm^{-2}. DFT calculations reveal that the introduced axial Fe-O coordination not only modifies the electron structures of Fe single atoms and facilitates the ORR procedure but also inhibits the demetallization of Fe single atomic active sites and eventually enhances the stability of Fe-SAC. The high performance and stability will facilitate its potential use in practical and commercial applications. In addition, we believe that the present strategy can be easily translated into the rational design and fabrication of ORR catalysts with both high activity and stability for eco-friendly and future-oriented energy techniques.

CRediT authorship contribution statement

Qingqing Wang: Investigation, Data curation, Visualization, Writing – original draft. Xiaohong Gao and Jieli Chen: Investigation, Data curation. Xianghui Wang: Formal analysis. Wenjun Fan and Guifa Long: Formal analysis, Software. Dulin Kong: Investigation, Writing – original draft. Chenghang You and Xinlong Tian: Conceptualization, Funding acquisition, Writing – review & editing, Supervision.

Declaration of Competing Interest

The authors declare that they have no known competing financial interests or personal relationships that could have appeared to influence the work reported in this paper.

Data availability

Data will be made available on request.

Appendix A. Supporting information

Supplementary data associated with this article can be found in the online version at doi:10.1016/j.apcatb.2023.123009.

References

[1] D. Xue, P. Yuan, S. Jiang, Y. Wei, Y. Zhou, C.-L. Dong, W. Yan, S. Mu, J.-N. Zhang, Altering the spin state of Fe-N-C through ligand field modulation of single-atom sites boosts the oxygen reduction reaction, Nano Energy 105 (2023), 108020, https://doi.org/10.1016/j.nanoen.2022.108020.

[2] S. Ji, T. Liu, L. Leng, H. Liu, J. Zhang, M. Zhang, Q. Xu, J. Zhu, M. Qiao, Y. Wang, J. H. Horton, Z. Li, Protein-mediated synthesis of iron single atom electrocatalyst with highly accessible active sites for enhanced pH-universal oxygen reduction, Appl. Catal. B Environ. 320 (2023), 121987, https://doi.org/10.1016/j.apcatb.2022.121987.

[3] Z. Zhuang, L. Xia, J. Huang, P. Zhu, Y. Li, C. Ye, M. Xia, R. Yu, Z. Lang, J. Zhu, L. Zheng, Y. Wang, T. Zhai, Y. Zhao, S. Wei, J. Li, D. Wang, Y. Li, Continuous modulation of electrocatalytic oxygen reduction activities of single-atom catalysts through p-n junction rectification, Angew. Chem. Int. Ed. 65 (5) (2022), e202212335, https://doi.org/10.1002/anie.202212335.

[4] X. Bao, M. Zhang, Z. Wang, D. Dai, P. Wang, H. Cheng, Y. Liu, Z. Zheng, Y. Dai, B. Huang, Molten-salt assisted synthesis of Cu clusters modified TiO2 with oxygen vacancies for efficient photocatalytic reduction of CO2 to CO, Chem. Eng. J. 445 (2022), https://doi.org/10.1016/j.cej.2022.136718.

[5] S.-N. Zhao, J.-K. Li, R. Wang, J. Cai, S.-Q. Zang, Electronically and geometrically modified single-atom Fe sites by adjacent fe nanoparticles for enhanced oxygen reduction, Adv. Mater. 34 (5) (2022) 2107291, https://doi.org/10.1002/adma.202107291.

[6] K.-M. Zhao, S. Liu, Y.-Y. Li, X. Wei, G. Ye, W. Zhu, Y. Su, J. Wang, H. Liu, Z. He, Z.-Y. Zhou, S.-G. Sun, Insight into the mechanism of axial ligands regulating the catalytic activity of Fe-N-4 sites for oxygen reduction reaction, Adv. Energy Mater. 12 (11) (2022) 2103588, https://doi.org/10.1002/aenm.202103588.

[7] M. Zhang, H. Li, J. Chen, F.-X. Ma, L. Zhen, Z. Wen, C.-Y. Xu, High-loading Co single atoms and clusters active sites toward enhanced electrocatalysis of oxygen reduction reaction for high-performance Zn–air battery, Adv. Funct. Mater. 33 (4) (2022) 2209726, https://doi.org/10.1002/adfm.202209726.

[8] H. Xie, X. Xie, G. Hu, V. Prabhakaran, S. Saha, L. Gonzalez-Lopez, A.H. Phakatkar, M. Hong, M. Wu, R. Shahbazian-Yassar, V. Ramani, M.I. Al-Sheikhly, D.-e. Jiang, Y. Shao, L. Hu, Ta-TiOx nanoparticles as radical scavengers to improve the durability of Fe-N-C oxygen reduction catalysts, Nat. Energy 7 (3) (2022) 281–289, https://doi.org/10.1038/s41560-022-00988-w.

[9] C. Xia, Y. Zhou, C. He, A.I. Douka, W. Guo, K. Qi, B.Y. Xia, Recent advances on electrospun nanomaterials for zinc–air batteries, Small Sci. 1 (9) (2021) 2100010, https://doi.org/10.1002/smsc.202100010.

[10] H. Chen, Y. Zhou, W. Guo, B.Y. Xia, Emerging two-dimensional nanocatalysts for electrocatalytic hydrogen production, Chin. Chem. Lett. 33 (4) (2022) 1831–1840, https://doi.org/10.1016/j.cclet.2021.09.034.

[11] H. Niu, C. Xia, L. Huang, S. Zaman, T. Maiyalagan, W. Guo, B. You, B.Y. Xia, Rational design and synthesis of one-dimensional platinum-based nanostructures for oxygen-reduction electrocatalysis, Chin. J. Catal. 43 (6) (2022) 1459–1472, https://doi.org/10.1016/S1872-2067(21)63862-7.

[12] Q. Liu, R. Liu, C. He, C. Xia, W. Guo, Z.-L. Xu, B.Y. Xia, Advanced polymer-based electrolytes in zinc–air batteries, eScience 2 (5) (2022) 453–466, https://doi.org/10.1016/j.esci.2022.08.004.

[13] L. Yang, J. Bai, W. Liu, X. Kan, G. Lin, Y. Zhang, Z. Chen, J. Gao, H. Zhou, J. Liu, Synthesis of atomic platinum with high loading on metal-organic sulfide, Sci. China Mater. 65 (5) (2022) 1294–1302, https://doi.org/10.1007/s40843-021-1848-8.

[14] J. Yang, W.-H. Li, K. Xu, S. Tan, D. Wang, Y. Li, Regulating the tip effect on single-atom and cluster catalysts: forming reversible oxygen species with high efficiency in chlorine evolution reaction, Angew. Chem. Int. Ed. 134 (16) (2022), e202200366, https://doi.org/10.1002/anie.202200366.

[15] Z. Wang, X. Liao, M. Zhou, F. Huang, K.A. Owusu, J. Li, Z. Lin, Q. Sun, X. Hong, C. Sun, Y.-B. Cheng, Y. Zhao, L. Mai, Interfacial and vacancies engineering of

copper nickel sulfide for enhanced oxygen reduction and alcohols oxidation activity, Energy Environ. Mater. (2022), https://doi.org/10.1002/eem2.12409.

[16] Y. Pan, X. Ma, M. Wang, X. Yang, S. Liu, H.-C. Chen, Z. Zhuang, Y. Zhang, W.-C. Cheong, C. Zhang, X. Cao, R. Shen, Q. Xu, W. Zhu, Y. Liu, X. Wang, X. Zhang, W. Yan, J. Li, H.M. Chen, C. Chen, Y. Li, Construction of N, P Co-doped carbon frames anchored with Fe single atoms and Fe2P nanoparticles as a robust coupling catalyst for electrocatalytic oxygen reduction, Adv. Mater. 34 (29) (2022) 2203621, https://doi.org/10.1002/adma.202203621.

[17] X. Xu, X. Zhang, Z. Kuang, Z. Xia, A.I. Rykov, S. Yu, J. Wang, S. Wang, G. Sun, Investigation on the demetallation of Fe-N-C for oxygen reduction reaction: The influence of structure and structural evolution of active site, Appl. Catal. B 309 (2022), 121290, https://doi.org/10.1016/j.apcatb.2022.121290.

[18] D. Xia, C. Yu, Y. Zhao, Y. Wei, H. Wu, Y. Kang, J. Li, J. Gan, F. Kang, Degradation and regeneration of Fe-N-x active sites for the oxygen reduction reaction: the role of surface oxidation, Fe demetallation and local carbon microporosity, Chem. Sci. 12 (34) (2021) 11576–11584, https://doi.org/10.1039/d1sc03754d.

[19] K.-M. Zhao, S. Liu, Y.-Y. Li, X. Wei, G. Ye, W. Zhu, Y. Su, J. Wang, H. Liu, Z. He, Z.-Y. Zhou, S.-G. Sun, Insight into the mechanism of axial ligands regulating the catalytic activity of Fe–N4 sites for oxygen reduction reaction, Adv. Energy Mater. 12 (11) (2022) 2103588, https://doi.org/10.1002/aenm.202103588.

[20] P. Chen, P. Zhang, X. Kang, L. Zheng, G. Mo, R. Wu, J. Tai, B. Han, Efficient electrocatalytic reduction of CO2 to ethane over nitrogen-doped Fe2O3, JACS 144 (32) (2022) 14769–14777, https://doi.org/10.1021/jacs.2c05373.

[21] J. Yang, P. Li, X. Li, L. Xie, N. Wang, H. Lei, C. Zhang, W. Zhang, Y.-M. Lee, W. Zhang, R. Cao, S. Fukuzumi, W. Nam, Crucial roles of a pendant imidazole ligand of a cobalt porphyrin complex in the stoichiometric and catalytic reduction of dioxygen, Angew. Chem. Int. Ed. 61 (34) (2022), e202208143, https://doi.org/10.1002/anie.202208143.

[22] L.S. Peng, J. Yang, Y.Q. Yang, F.R. Qian, Q. Wang, D. Sun-Waterhouse, L. Shang, T.R. Zhang, G.I.N. Waterhouse, Mesopore-Rich Fe-N-C catalyst with FeN4-O-NC single-atom sites delivers remarkable oxygen reduction reaction performance in alkaline media, https://doi.org/Artn 2202544, Adv. Mater. 34 (29) (2022) 2202544, https://doi.org/10.1002/Adma.202202544.

[23] X.-Y. Zhou, C. Xu, P.-P. Guo, W.-L. Sun, P.-J. Wei, J.-G. Liu, Axial ligand coordination tuning of the electrocatalytic activity of iron porphyrin electrografted onto carbon nanotubes for the oxygen reduction reaction, Chem. A Eur. J. 27 (38) (2021) 9898–9904, https://doi.org/10.1002/chem.202100736.

[24] F. Wang, Y. Zhou, S. Lin, L. Yang, Z. Hu, D. Xie, Axial ligand effect on the stability of Fe–N–C electrocatalysts for acidic oxygen reduction reaction, Nano Energy 78 (2020), 105128, https://doi.org/10.1016/j.nanoen.2020.105128.

[25] K. Chen, K. Liu, P. An, H. Li, Y. Lin, J. Hu, C. Jia, J. Fu, H. Li, H. Liu, Z. Lin, W. Li, J. Li, Y.-R. Lu, T.-S. Chan, N. Zhang, M. Liu, Iron phthalocyanine with coordination induced electronic localization to boost oxygen reduction reaction, Nat. Commun. 11 (1) (2020) 4173, https://doi.org/10.1038/s41467-020-18062-y.

[26] Y. Han, Y. Wang, R. Xu, W. Chen, L. Zheng, A. Han, Y. Zhu, J. Zhang, H. Zhang, J. Luo, C. Chen, Q. Peng, D. Wang, Y. Li, Electronic structure engineering to boost oxygen reduction activity by controlling the coordination of the central metal, Energy Environ. Sci. 11 (9) (2018) 2348–2352, https://doi.org/10.1039/C8EE01481G.

[27] S. Wu, X. Liu, H. Mao, T. Cui, B. Li, G. Zhou, L. Wang, Realizing high-efficient oxygen reduction reaction in alkaline seawater by tailoring defect-rich hierarchical heterogeneous assemblies, Appl. Catal. B 330 (2023), 122634, https://doi.org/10.1016/j.apcatb.2023.122634.

[28] S. Zhang, Q. Zhou, L. Fang, R. Wang, T. Lu, Q. Zhao, X. Gu, S. Tian, L. Xu, H. Pang, J. Yang, Y. Tang, S. Sun, Gram-scale synthesis and unraveling the activity origin of atomically dispersed Co-N4O sites toward superior electrocatalytic oxygen reduction, Appl. Catal. B 328 (2023), 122489, https://doi.org/10.1016/j.apcatb.2023.122489.

[29] S. Ji, T. Liu, L. Leng, H. Liu, J. Zhang, M. Zhang, Q. Xu, J. Zhu, M. Qiao, Y. Wang, J.H. Horton, Z. Li, Protein-mediated synthesis of iron single atom electrocatalyst with highly accessible active sites for enhanced pH-universal oxygen reduction, Appl. Catal. B 320 (2023), 121987, https://doi.org/10.1016/j.apcatb.2022.121987.

[30] D. Fan, Y. Lu, H. Zhang, H. Xu, C. Lu, Y. Tang, X. Yang, Synergy of photocatalysis and photothermal effect in integrated 0D perovskite oxide/2D MXene heterostructures for simultaneous water purification and solar steam generation, Appl. Catal., B 295 (2021), 120285, https://doi.org/10.1016/j.apcatb.2021.120285.

[31] Y. Wang, Y.-J. Tang, K. Zhou, Self-adjusting activity induced by intrinsic reaction intermediate in Fe–N–C single-atom catalysts, JACS 141 (36) (2019) 14115–14119, https://doi.org/10.1021/jacs.9b07712.

[32] Z. Chen, A. Huang, K. Yu, T. Cui, Z. Zhuang, S. Liu, J. Li, R. Tu, K. Sun, X. Tan, J. Zhang, D. Liu, Y. Zhang, P. Jiang, Y. Pan, C. Chen, Q. Peng, Y. Li, Fe1N4–O1 site with axial Fe–O coordination for highly selective CO2 reduction over a wide potential range, Energy Environ. Sci. 14 (6) (2021) 3430–3437, https://doi.org/10.1039/D1EE00569C.